

# Conducting Carbon Rich Graphitic Carbon Nitride Nanosheets with Attached Nano Sulfur Copolymer as High Capacity Cathode for Long-Lifespan Lithium-Sulfur Battery

Rupesh K. Tiwari,<sup>[a]</sup> Shishir K. Singh,<sup>[a]</sup> Nitin Srivastava,<sup>[a]</sup> Raghvendra Mishra,<sup>[a]</sup> Dipika Meghnani,<sup>[a]</sup> Anupam Patel,<sup>[a]</sup> Anurag Tiwari,<sup>[a]</sup> Vimal K. Tiwari,<sup>[a]</sup> and Rajendra K. Singh\*<sup>[a]</sup>

A mesoporous, conducting, high specific surface area, carbon-rich graphitic carbon nitride (GCN) nanosheets host covered by nano sulfur copolymer has been reported as a cathode material that shows high capacity along with long cyclability for rechargeable lithium-sulfur batteries (LiSBs). The thermal pyrolysis technique has been used for carbon-rich GCN sheets synthesis, and the chemical deposition approach has been used to attach surface nanoparticles to the sheets. Further, to improve the binding of nano sulfur with host material, copolymerization of nano sulfur is carried out with help of 1,3-diethynylbenzene (DEB) monomer through the solution route. The sulfur nanoparticles are loaded on conducting carbon-rich

GCN framework for fast electro kinematics and further copolymerization of sulfur nanoparticles is done to prevent the dissolution of the active material (sulfur) into the electrolyte during the charging/discharging for high capacity and long cycle life rechargeable LiSBs cathode preparation. The synthesized composite with high sulfur loading (~76 wt.% of composite cathode material) as cathode shows an initial discharge capacity of ~1380 mAh g<sup>-1</sup> at 0.1 C and a good discharge capacity of ~700 mAh g<sup>-1</sup> after 1000 cycles at 1 C with ultra-low-capacity fading ~0.016% of the initial capacity in each cycle.

## Introduction

The limited availability, day by day increasing demand, and indiscriminate exploitation of conventional non-renewable energy sources (fossil fuels) are causing rapid depletion of their reserves. Moreover, the huge demand of portable electronic devices and electric and hybrid-electric vehicles requires a vast number of cost-effective, durable, green, efficient, and renewable energy sources like solar, wind, hydropower energy, etc.<sup>[1–7]</sup> These renewable energy sources are green and environmentally friendly, but their intermittent nature makes them unsuitable as sustainable energy sources. The feasible solution for this problem can be implemented by coupling intermittent renewable energy sources with suitable energy storage devices. Lithium-ion batteries (LiBs) are efficient energy storage devices, which have currently taken the lead in the area of energy storage due to their reliability, long cycle life, high energy density, and cost-effectiveness in comparison to the conventional lead-acid and other energy storage devices which are commercially available in the market.<sup>[8–10]</sup> However, the com-

mercially available conventional ion intercalation/deintercalation compounds such as LiFePO<sub>4</sub>, LiNiMnCoO<sub>2</sub>, LiNiCoAlO<sub>2</sub>, and LiCoO<sub>2</sub>, etc, for LiBs have several environmental as well as economic issues.<sup>[6,11–14]</sup> The use of costly and toxic heavy metals (Co, Ni, Mn, etc), limited capacity (practically ~170 to 280 mAh g<sup>-1</sup>), and energy density (~200 Wh kg<sup>-1</sup> for single-cell) impede their use in stationary as well as portable energy storage devices.<sup>[7,15–18]</sup> Majority of electric vehicles in the market are propelled by LiBs, but, the low energy density of LiBs limits the driving range of these electric vehicles. Therefore, to improve the driving range and power of electric vehicles, the development of high energy density power sources is needed which moves this technology beyond conventional LiBs.

In this context, lithium-sulfur batteries (LiSBs) have emerged as a remarkable candidate for the above requirements due to their outstanding theoretical energy density (~2600 Wh kg<sup>-1</sup>) and extremely high theoretical specific capacity (~1675 mAh g<sup>-1</sup>).<sup>[10,19]</sup> In the last few years, lithium-sulfur battery technology has drawn considerable attention from both, researchers and the industrial community due to the low cost, good compatibility with the environment and high abundance of sulfur. Despite such inviting superiority, LiSBs have several deleterious disadvantages like poor conductivity of sulfur (of order 10<sup>-30</sup> S cm<sup>-1</sup>), its discharge products (polysulfides, of order 10<sup>-7</sup> S cm<sup>-1</sup>), volume expansion during a sluggish electrochemical redox reaction, dissolution of intermediate polysulfides and poor cyclability.<sup>[14,20–22]</sup> In order to resolve the mentioned issues in LiSBs, rigorous efforts have been made in the area of protection of anode, developments in the electro-

[a] R. K. Tiwari, S. K. Singh, N. Srivastava, R. Mishra, D. Meghnani, A. Patel, A. Tiwari, Dr. V. K. Tiwari, Prof. R. K. Singh  
Ionic Liquid and Solid-State Ionics Laboratory  
Department of Physics, Institute of Science  
Banaras Hindu University  
Varanasi-221005, India  
E-mail: rksingh\_17@rediffmail.com  
rajendrasingh.bhu@gmail.com

 Supporting information for this article is available on the WWW under  
<https://doi.org/10.1002/batt.202200282>

lyte, designing of novel conducting cathode materials to bind the sulfur, improving the capacity and cyclability. In the area of development of cathode, the technique of encapsulation of sulfur in different conducting and porous host matrices such as meso- and microporous carbons, metal oxide framework, and covalent organic framework is commonly used due to their attractive properties like excellent electrical conductivity with high specific surface area.<sup>[23–32]</sup> These conducting host materials enhance the conductivity and suppress polysulfide dissolution by capturing sulfur in its porous structure and provide high capacity, long cycle life for rechargeable LiSBs.<sup>[33]</sup> But, these meso- and microporous carbon materials participate in only the physical confinement of sulfur. However, without chemical interaction between sulfur and conducting host, dissolution of active materials in electrolytes occurs, which results fast capacity fading.<sup>[34–36]</sup> Hence, the majority of works are focused on either to modify host materials by doping of heteroatoms in carbonic materials or to develop new host materials, which contain electronegative atoms and polar functional groups in its structure as host materials to bind the sulfur in LiSBs cathode.<sup>[17,37,38]</sup> In recent years, the controlled copolymerization of sulfur is also used as an effective way to prevent the dissolution of the active material in the electrolyte, which is helpful to improve the capacity retention. The polyacrylonitrile (PAN) based polymeric sulfur as sulfur cathode has been reported for the first time by Wang et al. in 2002, which delivered  $\sim 850 \text{ mAh g}^{-1}$  in its first cycle and maintained  $\sim 600 \text{ mAh g}^{-1}$  after 50 cycles.<sup>[39]</sup> Subsequently, the use of sulfur-rich sulfur copolymers as a cathode material in LiSBs has been increased significantly.<sup>[35,40,41]</sup>

Various conducting carbonaceous cathode hosts such as bio-derived carbons, ketjen black, activated charcoals, reduced graphene oxide (RGO), single and multiwall carbon nanotubes, carbon nanofiber etc, are reported for LiSBs.<sup>[42–47]</sup> In 2019, Zhu, et al. reported ketjen black and sulfur composite as cathode, which delivered high initial capacity of  $1169 \text{ mAh g}^{-1}$  and  $\sim 1046 \text{ mAh g}^{-1}$  at 0.1 C and 1 C, respectively. However, due to lack of chemical interaction between intermediate polysulfide and host, it dropped to  $\sim 472 \text{ mAh g}^{-1}$  after 500 cycles even though an activated puffed corn derived carbon coated celgard 2400 separator was used as polysulfide mediator to prevent polysulfide dissolution by physical adsorption.<sup>[48]</sup> To solve this problem, doping of heteroatoms, especially nitrogen in the carbon host material comes into play. In 2018, Lu et al. developed a nitrogen doped carbon comb (NCC) host and they found that the nitrogen doping effectively suppressed the polysulfide dissolution and provided stable lithium sulfur cell, which delivered initial reversible capacity of  $1090 \text{ mAh g}^{-1}$  at 0.1 C and  $562 \text{ mAh g}^{-1}$  at 1 C after 300 cycles.<sup>[49]</sup> Thus, the doping of heteroatom and copolymerization of sulfur are two important and effective ways to suppress the dissolution of active material in LiSBs.

The graphitic carbon nitride (GCN) a two-dimensional (2D) organic material with a graphite-like structure, has drawn appreciable attention due to its high nitrogen content, excellent thermal and chemical stability, fascinating electronic structure, and environment-friendly nature. Thus, it leads to

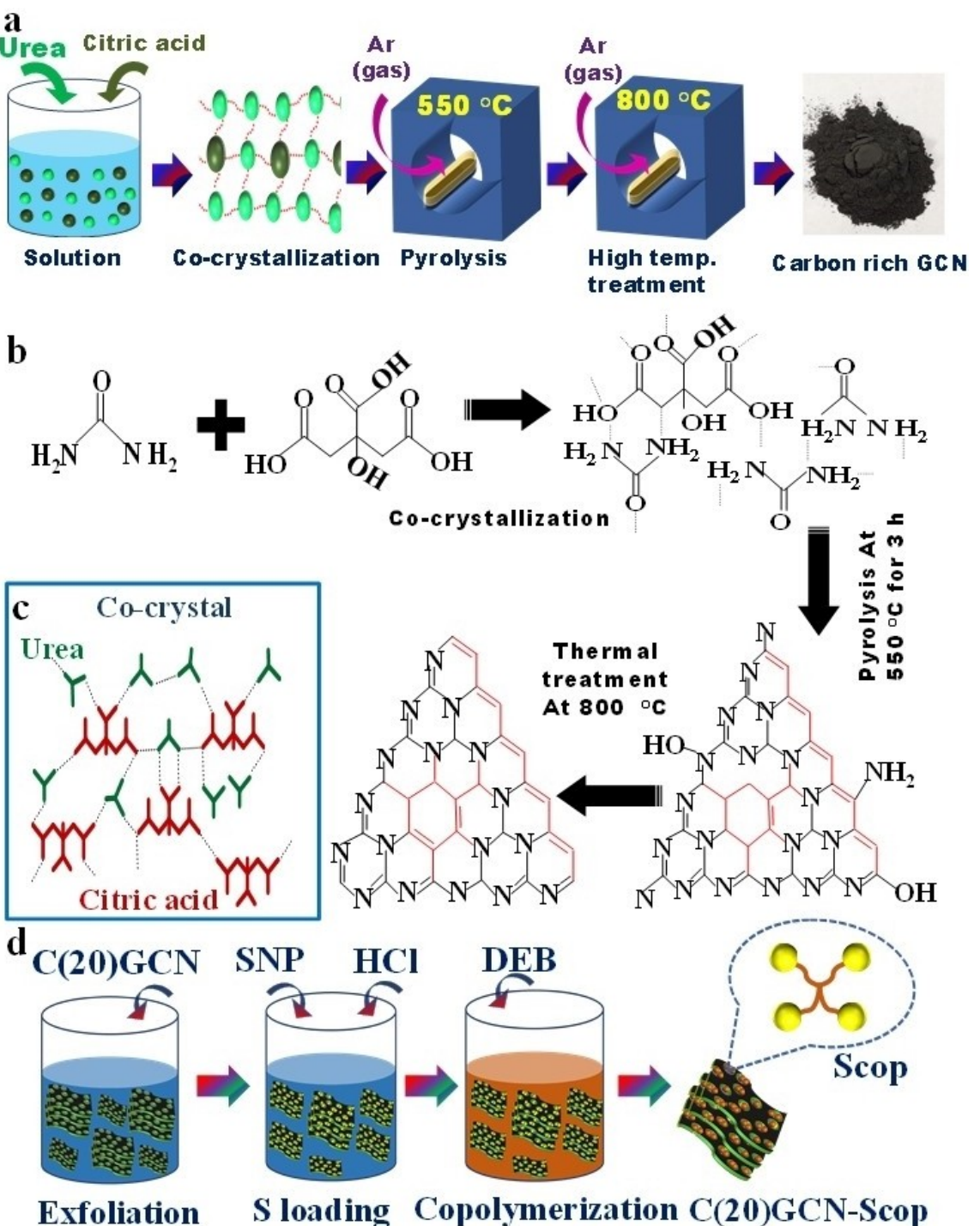
mulfunctional activities such as use in energy storage devices, water filtration, and other photocatalysis processes.<sup>[50–56]</sup> The nitrogen in carbon host matrix is usually found in three different states named as quaternary, pyrrolic, and pyridinic nitrogen, which has several advantages in electrochemical devices. Especially, in LiSBs, it improves the chemical interaction between intermediate polar polysulfides and the host matrix as well as the interaction of sulfur with functional groups and heteroatoms in the carbon matrix.<sup>[57]</sup> This results in the formation of thiosulfate and sulfate species in the carbon matrix and the uniform distribution of sulfur throughout the host matrix.<sup>[58]</sup> The lithium (Li) cations in  $\text{Li}_2\text{S}_n$  bind directly with lone pair electrons of electron-rich pyrrolic and pyridinic nitrogen atoms present in the nitrogen (N) doped carbon, resulting in strong Li–N interaction.<sup>[59]</sup> However, the application of GCN possesses the inherent low electronic conductivity and low surface area, which inhibit its application in electrochemical devices. Because of these limitations, GCN is mostly used as polysulfide mediator instead of a host of sulfur in cathode materials for LiSBs. Jinghai et al. reported oxygenated graphitic carbon nitride cathode, and Zhen et al. reported graphitic carbon nitride cathode for LiSBs with good electrochemical results at low current rates. However, the electrochemical performance of above cathodes at high current rates is not satisfactory due to poor conductivity.<sup>[37,58]</sup>

Present work is aimed to overcome aforementioned limitations of LiSBs by utilizing the virtues of GCN. Here, the poor conducting GCN is modified to carbon-rich conducting GCN by enhancing  $\text{sp}^2$  hybridized carbon in the aromatic ring of GCN in a controlled manner. For a cost-effective and environmentally friendly synthesis of carbon-rich GCN, citric acid is employed as a carbon source and urea as a GCN precursor (Scheme 1). The sulfur nanoparticles are embedded in conducting carbon-rich GCN nanosheets for fast electro kinematics and, further, copolymerization of nano active material is done to prevent dissolution of sulfur into the electrolyte during charging/discharging. The above efforts have resulted in high capacity rechargeable LiSBs cathode material, which initially delivers 1387, 1139, 979, 840, and  $614 \text{ mAh g}^{-1}$  capacities at the current rate 0.1 C, 0.2 C, 0.5 C, 1 C, and 2 C, respectively. The prepared cell also shows good cyclability with high-capacity retention and it delivers  $\sim 840 \text{ mAh g}^{-1}$  at 1 C and retains  $\sim 700 \text{ mAh g}^{-1}$  discharge capacity after 1000 cycles.

## Results and Discussion

### Structural and thermal analysis of carbon-rich GCN host

The XRD patterns of synthesized pure GCN, C(5)GCN, C(10)GCN, C(15)GCN, and C(20)GCN are shown in Figure 1(a). In the pure GCN, two characteristic diffraction peaks are observed, one at  $27.6^\circ$  corresponds to the plane (002) and the other at  $13.1^\circ$  is related to the plane (100).<sup>[53,56]</sup> In carbon-rich samples C(5)GCN, C(10)GCN, C(15)GCN, and C(20)GCN, XRD peaks are shifting towards the lower 2 Theta side (towards the characteristic peak of reduced graphene oxide) with increase of carbon



**Scheme 1.** a) Schematic diagram of the synthesis of carbon-rich GCN. b) Chemical equation of synthesis of carbon-rich GCN. c) Schematic representation of co-crystal urea and citric acid. d) Schematic diagram of loading of sulfur (S) nanoparticle using EDA sulfur nano precursor (SNP) and its co-polymerization in C(20)GCN host matrix.

content.<sup>[14,53,60]</sup> This shift in peak is due to the replacement of nitrogen (N) by carbon (C) in aromatic ring structure of GCN. Thus, XRD results confirm that the graphitic nature of carbon-rich samples increases with increase in carbon content.

The thermal behaviour of all synthesized materials is investigated by the thermogravimetric analysis (TGA) technique within the temperature range 30 °C to 850 °C under an inert

atmosphere (continuous N<sub>2</sub> flow 50 ml min<sup>-1</sup>) at a heating rate of 10 °C min<sup>-1</sup>. The TGA curves (Figure 1b) show that pure GCN, C(5)GCN, C(10)GCN, C(15)GCN, and C(20)GCN all are thermally stable up to 520 °C. A small weight loss below 400 °C is observed due to the removal of water moieties and weakly attached functional groups. The pristine GCN decomposition starts from 521 °C and it is completely decomposed at 750 °C

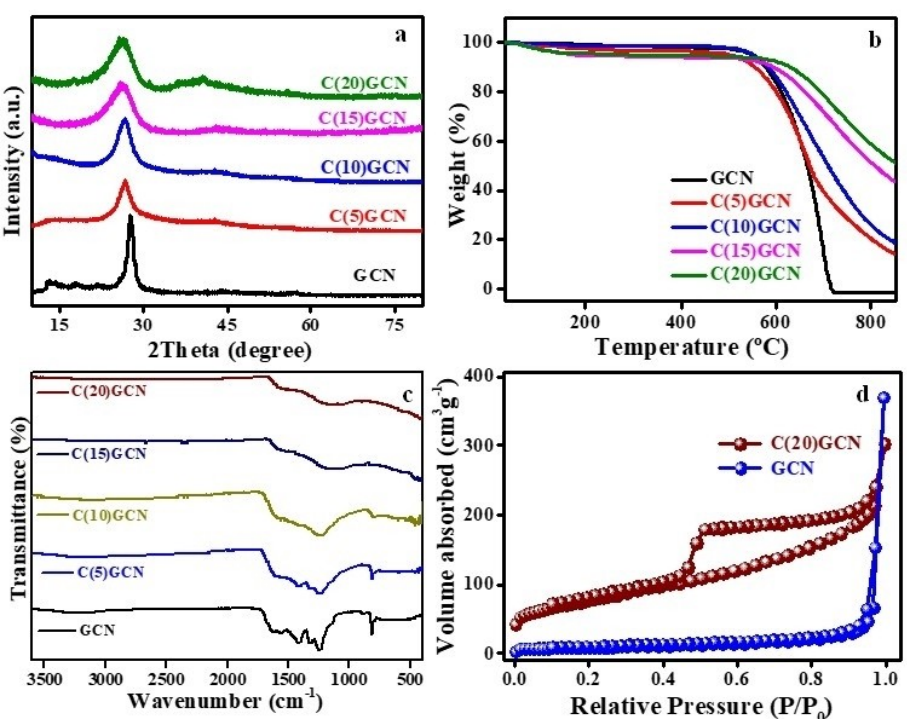


**Figure 1.** a) X-ray diffraction patterns of synthesized GCN, C(5)GCN, C(10)GCN, C(15)GCN, and C(20)GCN. b) Thermogravimetric analysis of synthesized; GCN, C(5)GCN, C(10)GCN, C(15)GCN, and C(20)GCN. c) FTIR spectra of GCN, C(5)GCN, C(10)GCN, C(15)GCN, and C(20)GCN. d)  $N_2$  adsorption-desorption isotherm of GCN and C(20)GCN.

(i.e., nothing of GCN is leftover and it is completely transferred into  $CO_2$ ,  $CO$ ,  $NO_2$ , etc), while the TGA results of carbon-rich nitride samples show approximately 14, 19, 44, and 52 wt.% residues remained in GCN, C(5)GCN, C(10)GCN, C(15)GCN, and C(20)GCN, respectively. The high content of residue is obtained with increase in the amount of citric acid during the synthesis of C( $x$ )GCN, showing a higher percentage of crosslinked carbon.

The Fourier transform infrared (FTIR) spectroscopy of GCN, C(5)GCN, C(10)GCN, C(15)GCN, and C(20)GCN is used to investigate the change in chemical bonding and surface functionalities as shown in Figure 1(c). The peak at  $\sim 806\text{ cm}^{-1}$  in pristine GCN corresponds to the breathing vibration of the CN bond in triazine units of condensed CN heterocycles. The intensity of this triazine peak starts decreasing from pristine GCN to carbon-rich C( $x$ )GCN ( $x=5, 10, 15, 20\text{ wt.\%}$ ), which indicates that carbon atoms from the carbon source start reacting with highly reactive amine group during the thermal pyrolysis of urea in presence of citric acid. Furthermore, strong bands at  $\sim 1411, 1485, 1567$ , and  $1622\text{ cm}^{-1}$  are observed in pristine GCN, which correspond to stretching vibration modes of heptazine derived units.<sup>[61–63]</sup> The bands corresponding to stretching vibration of partial condensation (C—NH—C) or full condensation (C—N(—C)—C) at  $\sim 1240$  and  $1330\text{ cm}^{-1}$  are observed in pristine GCN. Due to decrement in nitrogen content in carbon-rich samples, the intensities of above mentioned peaks arising due to stretching vibration modes of heptazine derived units and full or partial condensation units decrease continuously with enhancement of carbon ratio in the synthesized material (C(20)GCN). The above-mentioned FTIR

results reconfirm XRD and TGA results verify the successful synthesis of carbon-rich GCN.

The  $N_2$  adsorption/desorption (BET) technique is used to evaluate the specific surface area, pore size, and pore volume of pristine GCN and C(20)GCN. As illustrated in Figure 1(d), the adsorption/desorption isotherms demonstrate that C(20)GCN ( $273\text{ m}^2\text{ g}^{-1}$ ) has a substantially greater BET surface area with an average pore diameter of  $\sim 6\text{ nm}$  than that of pure GCN ( $35\text{ m}^2\text{ g}^{-1}$ ) with an average pore diameter of  $\sim 60\text{ nm}$ . The enhancement in surface area arises due to sublimation of pure graphitic carbon nitride content during synthesis of C(20)GCN at  $800^\circ\text{C}$ , which creates porous structure in the final product C(20)GCN during heat treatment.<sup>[37,64]</sup> It is well known that in LiSBs, the host must have a porous structure with a high surface area for superior electrochemical properties.<sup>[5,65]</sup> The high surface area provides more active sites and resists collapse of host structure due to the volumetric expansion of sulfur (from sulfur  $\sim 2.0\text{ g cm}^{-3}$  to  $Li_2S \sim 1.6\text{ g cm}^{-3}$ ) arising due to the formation of intermediate polysulfides during the charging/discharging process.<sup>[14]</sup>

Raman spectra of synthesized GCN, C(5)GCN, C(10)GCN, C(15)GCN, and C(20)GCN is performed for investigation of enhancement of carbon content, its graphitic nature, and defects/disorders are shown in Figure 2(a). In the pristine GCN, a low intense broad peak at  $\sim 1364\text{ cm}^{-1}$  (Figure 2a) is observed instead of two distinct D and G bands, which indicates lack of  $sp^2$  hybridization (G-band) in it, due to which GCN behaves like poor conductor. While, two characteristic peaks of D and G bands are identified in synthesized C(5)GCN, C(10)GCN,

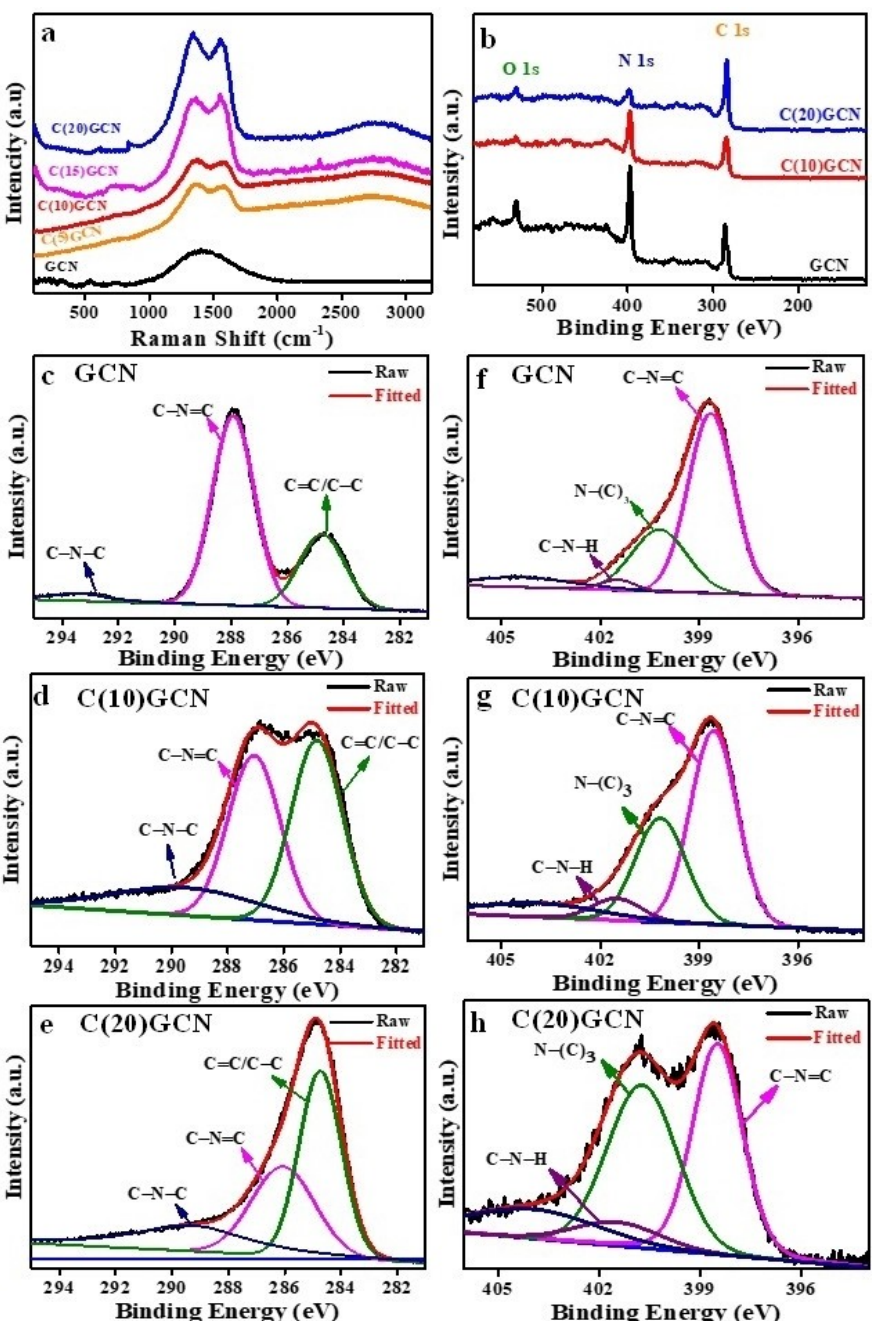


**Figure 2.** a) Raman spectra of GCN and C(5)GCN, C(10)GCN, C(15)GCN, and C(20)GCN. b) XPS survey spectra of GCN, C(10)GCN, and C(20)GCN. High-resolution C 1s spectra of c) GCN, d) C(10)GCN, and e) C(20)GCN. High-resolution N 1s spectra of f) GCN, g) C(10)GCN, and h) C(20)GCN.

C(15)GCN, and C(20)GCN at  $\sim 1339\text{ cm}^{-1}$  and  $\sim 1550\text{ cm}^{-1}$ , respectively. The G band that appeared in Raman spectra arises due to the stretching in the bond of  $\text{sp}^2$  hybridized carbon present in the ring and chain, while the D band is produced due to breathing modes in the aromatic ring activated by defects. In carbonic materials, these  $\text{sp}^2$  hybridized carbons and controlled defects are responsible for electrical conductivity.<sup>[14,38]</sup> The D and G bands explicitly appear in the Raman spectra with increase of carbon contents in the carbon-rich graphitic carbon nitride samples synthesized from 5 wt.% citric acid containing sample to 20 wt.% citric acid containing

sample, and the ratio ( $I_D/I_G$ ) of intensities  $I_D$  of D band and  $I_G$  of G band in C( $x$ )GCN is 1.01, 1.04, 1.08, and, 1.16 for  $x=5, 10, 15$ , and 20, respectively. The  $I_D/I_G$  ratio of C(20)GCN is significantly higher than the C(5)GCN, confirming sufficient number of defects present in the graphitic structure of C(20)GCN framework. The controlled defects are very helpful in fast ion conduction during electrochemical redox reactions. A broad peak appears at  $2843\text{ cm}^{-1}$  which corresponds to two-dimension band and it also increases in high carbon containing samples.

The chemical environment, and the relative composition variation of C, O, and N in the synthesized GCN, C(10)GCN, and C(20)GCN are investigated by using XPS measurement, as shown in Figure 2(b). The decrease in N 1s peak and increase in C 1s peak are clearly visible from GCN to C(20)GCN. The high-resolution C 1s spectra of pristine GCN (Figure 2c) show two main peaks at 288.0 eV and at 284.6 eV attributed to C=N-C and graphitic carbon C=C/C-C respectively and a small peak observed at 291.2 eV corresponds to C-N-C. With the increment of carbon doping in carbon-rich samples, the enhancement in the intensity of peak corresponding to  $sp^2$  graphitic carbon at 284.6 eV in C 1s spectra of C(10)GCN and C(20)GCN is observed (Figure 2d and e). While the opposite pattern is observed with the peak corresponding to C=N-C. With increasing carbon content, the ratio of nitrogen and carbon starts to decrease in carbon-rich samples C(10)GCN, and C(20)GCN, that's why the chemical environment and conductivity of samples start changing due to change in C and N ratio. The change in the conductivity and chemical environment of the samples affects the binding energies of C=N-C, and the high-resolution peak of C-N-C shifted towards the lower energy side with increase in carbon content. The percentage ratio of N and C is listed in Table S1 (ESI) and graphically represented in Figure S2(a) of ESI using C 1s XPS spectra of GCN, C(10)GCN, and C(20)GCN.<sup>[53,54,58]</sup>

After the de-convolution of the high-resolution N 1s spectra of synthesized GCN, C(10)GCN, and C(20)GCN, three peaks found at 401.3 eV, 400.3 eV, and 398.7 eV are assigned as graphitic N, pyrrolic N, and pyridinic N, respectively, which confirms the formation of C-N bond during pyrolysis of urea and citric acid as shown in Figure 2 (f-h).<sup>[54,58,66]</sup> Another broad and small peak at 402.5 eV observed in N 1s XPS spectra of GCN, C(10)GCN, and C(20)GCN corresponds to positive charge localization. From N 1s spectra, it is found that the pyrrolic N and pyridinic N increase in C(10)GCN (Figure 2g) and C(20)GCN (Figure 2h) in comparison with pristine GCN (Figure 2d). For a better interpretation of N 1s XPS spectra, the percentage contribution of different bonds is listed in tabular form in Table S2 of ESI. It is also demonstrated graphically in Figure S 2(b) of ESI. The pyrrolic and pyridinic N have high electron donating properties due to high electron density. These groups chemically attract the polar intermediate polysulfides and actively suppress its dissolution in electrolyte which enhances the cycle life of the prepared cell during electrochemical redox reactions.<sup>[25]</sup> The lone pair electrons of the nitrogen atom can form a strong interaction with a positive charge of Li in Li<sub>2</sub>S, exhibiting the polysulfide adsorption capability. In addition, the pyrrolic N can also provide the binding sites with lithium polysulfide species due to its  $\pi$  system with two-p electrons but offers a weaker interaction than pyridinic groups. The graphitic  $sp^2$  carbon atoms can introduce more delocalized electrons from their  $\pi$  bond into the system which enhances the electronic conductivity.<sup>[31,67-69]</sup> The superior high carbon containing C(20)GCN along with sufficient nitrogen-containing groups can act as high conducting host which has strong adsorption sites for trapping intermediate polysulfides during electrochemical redox reactions.

Therefore, the above discussion concludes that the prepared carbon-rich C(20)GCN shows high surface area and graphite nature with limited nitrogen presence which is suitable as host material to encapsulate sulfur for LiSBs cathode.

### Structural and thermal analysis of C(20)GCN nano-sulfur and C(20)GCN-Scop

In order to confirm the sulfur loading and its copolymerization, XRD of sulfur, and C(20)CGN-Scop is performed as shown in Figure 3(a). Due to the intense peaks of sulfur, it is difficult to detect broad peak related to C(20)GCN in the synthesized C(20)GCN sulfur composite. Before copolymerization of sulfur, the well-known crystalline peaks of orthorhombic sulfur (JCPDS-08-0247) are observed in the synthesized C(20)GCN nano-sulfur composite. Whereas, after copolymerization process, the crystalline peaks of sulfur are sufficiently reduced and becomes almost amorphous in nature in the C(20)GCN-Scop. The crystalline sulfur peak is not observed in the Raman trajectory of C(20)GCN-Scop (Figure S1 of electronic supporting information (ESI)) due to copolymerization of sulfur. This indicates that the absence of pristine crystalline sulfur inside C(20)GCN host in the synthesized C(20)GCN-Scop cathode material will prevent dissolution of sulfur during battery performance. Based on the TGA findings of C(20)GCN nano sulfur composite and C(20)GCN-Scop shown in Figure 3(b), the sulfur loading in C(20)GCN nano sulfur composite and C(20)GCN-Scop is ~81% and ~76%, respectively. The C(20)GCN nano sulfur composite shows a similar pattern as decomposition of pure sulfur, while in the copolymerized sample C(20)GCN-Scop, a slope is clearly observed in the temperature range 330 °C to 520 °C, which also confirmed the copolymerization of sulfur nanoparticles. So XRD, Raman, and TGA results confirm the complete polymerization of sulfur nanoparticles to sulfur copolymer along with high sulfur loading which will help to restrict dissolution of sulfur in electrolytes and enhance the LiSBs performance.

In XPS survey spectra of synthesized C(20)GCN-Scop cathode material, the peaks corresponding to sulfur, carbon, nitrogen, and oxygen are clearly observed (Figure 3c). After the de-convolution of the high-resolution C 1s spectra of C(20)GCN-Scop (Figure S3a of ESI) peak found at 288.0 eV is attributed to C=N-C and the peak at 284.6 eV is ascribed to the graphitic carbon C=C, C-C with a small peak observed at 291.2 eV C-N-C. While, in the high-resolution N 1s spectra of the cathode C(20)GCN-Scop all the peaks corresponding to graphitic N, pyrrolic N, pyridinic N, and positive charge localization are obtained similar to C(20)GCN at their respective positions (Figure S3b). A broad peak found from 161.5 eV to 166.5 eV is related to S 2p of C(20)GCN-Scop as shown in Figure 3(d). After its de-convolution (Figure 3d), two characteristic peaks at 163.7 eV and 164.7 eV corresponding to S 2p<sub>3/2</sub> and S 2p<sub>1/2</sub>, respectively, with an energy separation of 1.2 eV are observed. Moreover, the peaks S 2p<sub>1/2</sub> and S 2p<sub>3/2</sub> at 168.8 eV and 167.8 eV, respectively ascribe to doublet of sulfate

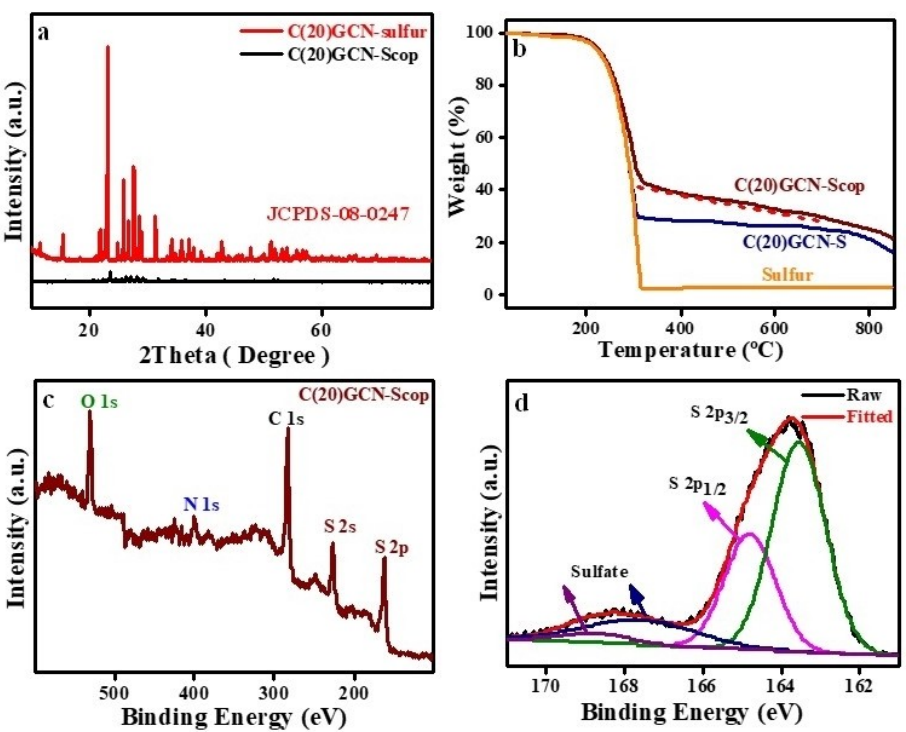


**Figure 3.** a) XRD analysis of C(20)GCN-sulfur and C(20)GCN-Scop. b) TGA analysis of sulfur, C(20)GCN nano sulfur composite, and C(20)GCN-Scop. c) XPS survey spectra of C(20)GCN-Scop. d) High-resolution S 2p XPS spectra of the C(20)GCN-Scop composite cathode material.

species which arise due to partial oxidation of sulfur during copolymerization of sulfur nanoparticles (Figure 3(d)).<sup>[41,67,70,71]</sup> Therefore, the prepared C(20)GCN-Scop as cathode shows high loading of sulfur and complete co-polymerization of sulfur which will help to restrict dissolution of sulfur and to get high capacity during LiSBs performance.

#### Surface morphology of GCN, C(20)GCN and C(20)GCN-Scop

The scanning electron microscopy (SEM) results reveal the structural morphology of synthesized GCN, C(20)GCN, and C(20)GCN-Scop as shown in Figure 4. In the SEM images, bunch of chunks is observed in pristine GCN (Figure 4a and b), while C(20)GCN clearly forms nanosheets like structure (Figure 4c and d). The SEM image of C(20)GCN-Scop cathode material reveals homogeneously mixed phases of C(20)GCN and Scop are observed in Figure 4(e and f), and it is difficult to differentiate sulfur and host C(20)GCN and confirms the uniform distribution of sulfur nanoparticles throughout the framework. Figure 5(a, e and i) shows the overall survey of elements C, N, O, and S of GCN, C(20)GCN and, C(20)GCN-Scop, respectively. Figure 5(b and c) reveals that, in GCN; N content is higher than the C content, while C content dominates in elemental mapping of C(20)GCN (Figure 5f and g). Similarly, C(20)GCN-Scop shows higher content of carbon compared to nitrogen as shown in Figure 5(j and k). This confirms that the synthesized C(20)GCN and C(20)GCN-Scop are carbon-rich in nature in comparison with pristine GCN (Figures S4–S6). The oxygen mapping is illustrated in Figure 5(d and h) for GCN and C(20)GCN,

respectively, and it is found that C(20)GCN contains slightly less oxygen than GCN due to the elimination of oxygen containing functional groups during high temperature treatment. The color mapping of S in synthesized C(20)GCN-Scop is shown in Figure 5(l) and confirms the sufficient amount of S loading uniformly throughout the cathode material (see EDS mapping in Figure S6). For a better understanding of the elements and their corresponding weights and atomic percentages in synthesized GCN, C(20)GCN, and C(20)GCN-Scop are tabulated in Table 1. This helps to figure out how the C and N ratio changes in GCN and carbon-rich C(20)GCN, and the presence of sulfur in the C(20)GCN-Scop composite. The irregular, bulk, and dense stacking layers of GCN are observed in transmission electron microscopy (TEM) images (Figure 6a–d), while TEM image of C(20)GCN (Figure 6e–h) and C(20)GCN-Scop (Figure 6i–l) shows nanosheets like structure. Since, the TEM measurement is performed at very low pressure ( $\sim 10^{-9}$  mbar), hence due to sublimation of sulfur nano particles, it is very difficult to get high-resolution image of the sulfur. Herein, uniformly distributed sulfur particles are clearly observed in the low as well as high-resolution TEM (HRTEM) images of synthesized C(20)GCN-Scop (Figure 6i–l). This shows that due to copolymerization, sulfur particles in the composite cathode material are highly stable. The fast Fourier transform (FFT) and inverse fast Fourier transform (IFFT) are performed using ImageJ software to investigate inter-planer distance obtained from the HRTEM of GCN, C(20)GCN, and C(20)GCN-Scop. In HRTEM investigation of GCN, first FFT is performed for selected area and two diffraction patterns corresponding to the plane (002) and (100) of GCN are obtained. The IFFT of the FFT patterns of pristine GCN

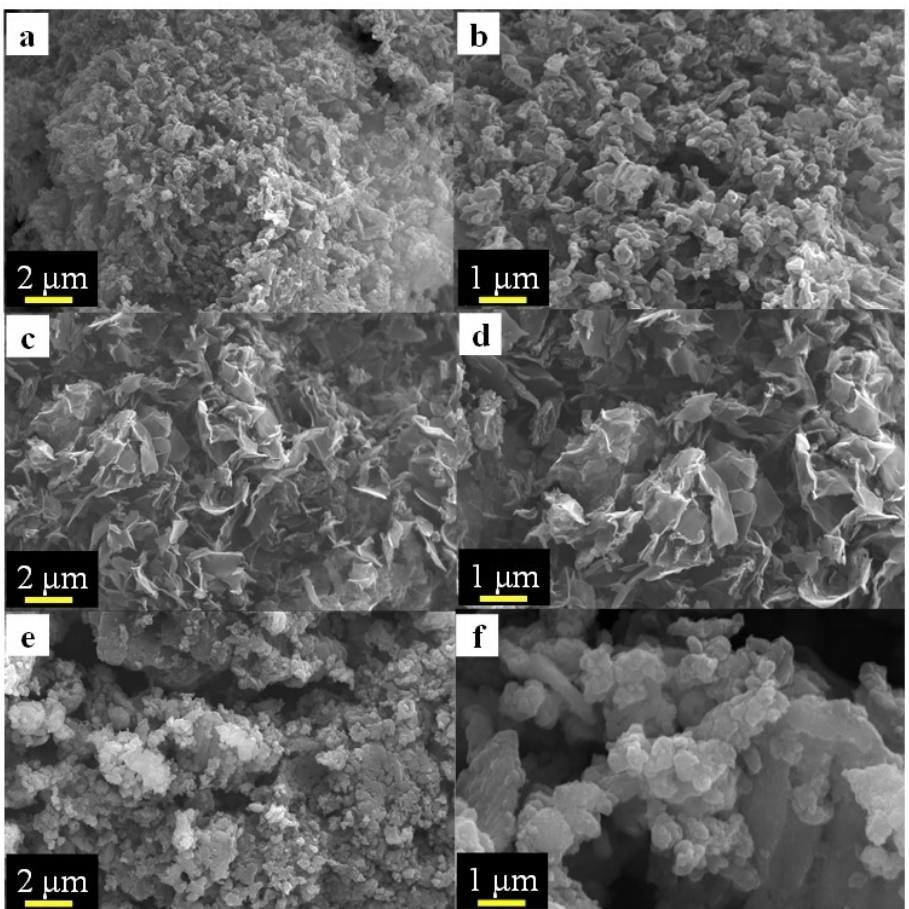


**Figure 4.** Scanning electron microscope (SEM) images of a and b) GCN, c and d) C(20)GCN, e and f) C(20)GCN-Scop at different magnifications.

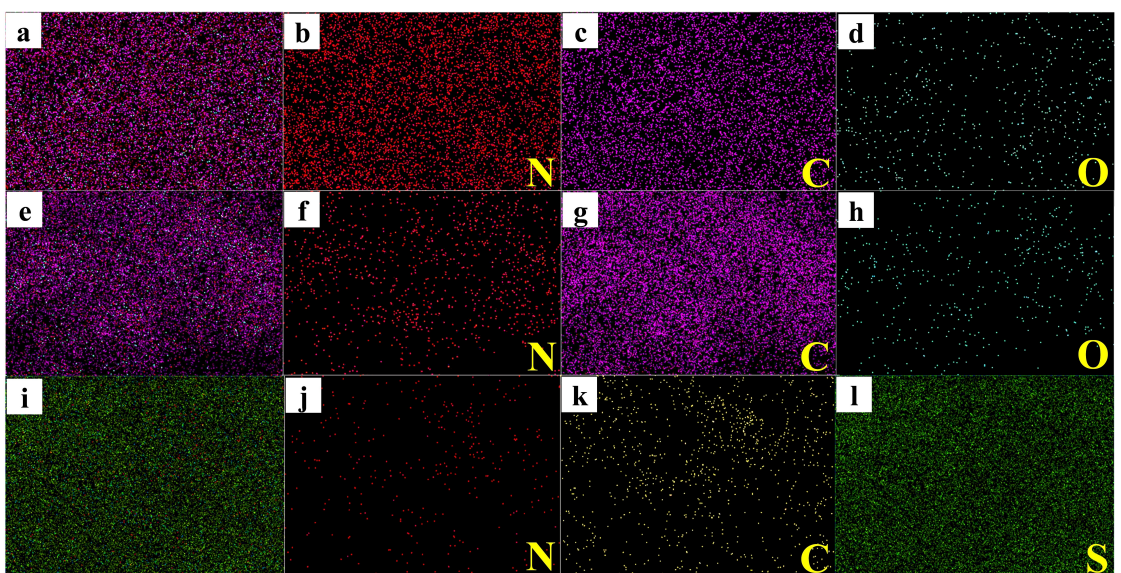


**Figure 5.** Elemental mapping of GCN: a) survey, b) N, c) C, and d) O. Elemental mapping of C(20)GCN: e) survey, f) N, g) C, and h) O. Elemental mapping of C(20)GCN-Scop: i) survey, j) N, k) C, and l) S.

possesses calculated average d-spacings  $d \sim 0.39$  and  $\sim 0.59$  nm, corresponding to (002) and (100) planes, respectively, which is shown in the inset of Figure 6(d). The IFFT of C(20)GCN shows

calculated average d-spacing  $d \sim 0.41$  nm (inset of Figure 6h) corresponds to (002) plane, reconfirming XRD results show that the characteristic XRD peaks of carbon-rich graphitic carbon

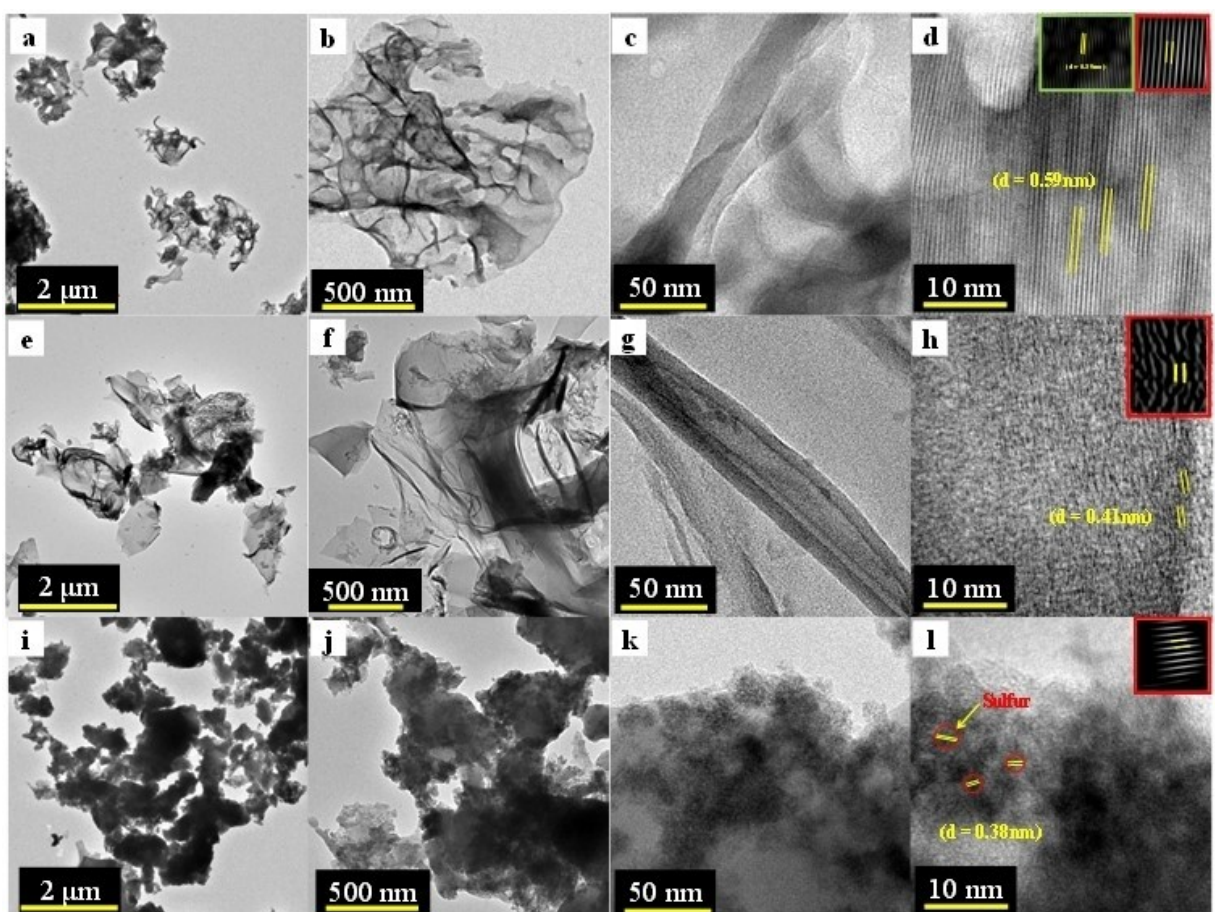


**Figure 6.** Transmission electron microscopy (TEM) images of a–c) GCN, e–g) C(20)GCN and i–k) C(20)GCN-Scop composite cathode at low and high magnifications. High-resolution TEM image (corresponding inverse FFT in inset) of d) GCN, h) C(20)GCN, and l) C(20)GCN-Scop.

nitrides samples C(5)GCN, C(10)GCN, C(15)GCN and C(20)GCN are slightly shifted towards the lower 2Theta that means d-spacing increase. The HRTEM image of the C(20)GCN-Scop is shown in Figure 6(l). It is challenging to capture high-resolution TEM images of the sulfur nanoparticles due to their rapid sublimation. Wang et al. and others have observed similar issues, and we were also unable to observe sulfur nanoparticles in HRTEM images in our prior study.<sup>[14,72]</sup> However, due to the co-polymerization of sulfur nanoparticles or confinement of amorphous sulfur in that region HRTEM picture (Figure 6l) of sulfur is successfully acquired in this study. Using the IFFT of the FFT diffraction patterns of the specified area of the HRTEM image of C(20)GCN-Scop, the d-spacing ( $d \sim 0.38$  nm) is computed which is corresponding to the (222) plane of sulfur.<sup>[72,73]</sup> When high energy electron beams are incident on composite under extremely low pressure during TEM measurement, there could be crystallization of amorphous sulfur in this region. However, there is clear evidence of crystalline sulfur inside the C(20)GCN framework in HRTEM, which is missing in XRD and Raman results. From SEM and TEM results, it is found that C(20)GCN shows nanosheet like structure which helps for better mixing with nano sulfur, whereas sulfur copolymer is uniformly distributed in C(20)GCN framework of C(20)GCN-Scop cathode.

#### Electrochemical performance of C(20)GCN-Scop cathode for LiSBs

The cyclic voltammetry (CV) of the fabricated coin cell with C(20)GCN-Scop as cathode is observed at a scan rate of  $0.1\text{ mV s}^{-1}$  between 1.0 and 3.0 V as shown in Figure 7(a). The two well-defined and prominent reduction peaks are observed at 1.99 V and 2.25 V in a typical CV curve of prepared cell during cathodic scan. It demonstrates that the reduction of elemental sulfur from  $\text{S}_8$  to final lithium sulfide  $\text{Li}_2\text{S}$  undergoes mainly in the following two steps. Initially, the peak at a higher potential 2.25 V corresponds to high order soluble long-chain polysulfides formation ( $\text{Li}_2\text{S}_n$ ,  $4 \leq n \leq 8$ ) and further reduces to low order insoluble lithium sulfides ( $\text{Li}_2\text{S}_n$ ,  $n \leq 2$ ) at a lower potential 1.99 V. During the oxidation process, lithium sulfide is transformed into sulfur element in two steps. In first step, it is converted into intermediate polysulfide at 2.48 V, and then it is further oxidized into sulfur at 2.55 V. In order to check electrochemical stability of the prepared cell, CV is performed continuously for six cycles. In the first cycle the peaks are less intense, which is due to less accessibility of sulfur copolymers and strong binding through CMC binder. Further in successive cycles, the peaks become more intense and show high current due to accessibility of more sulfur by the lithium ions during

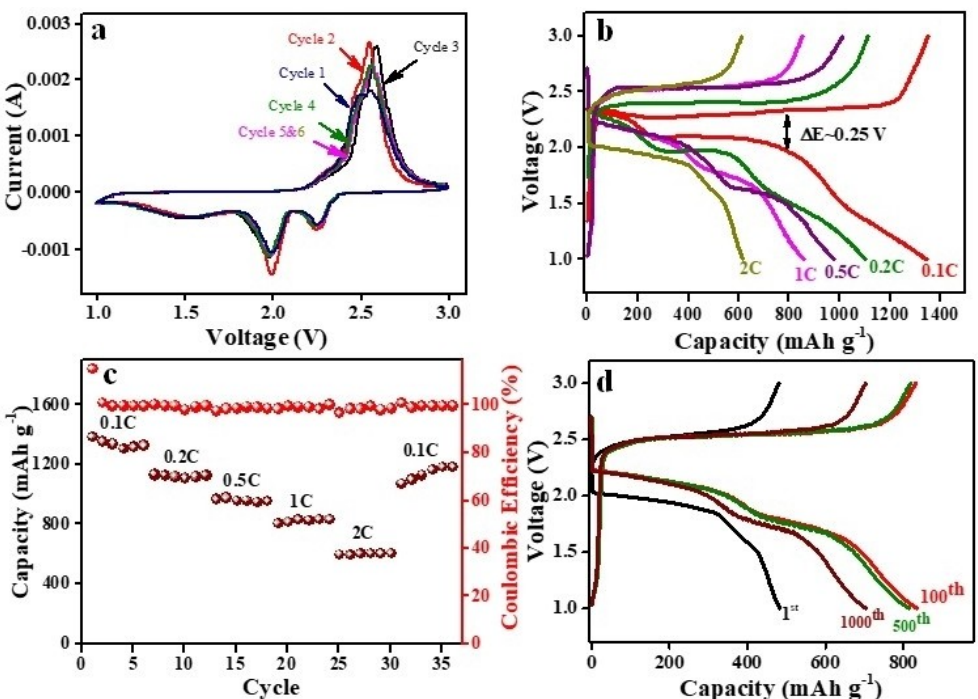


**Figure 7.** a) The cyclic voltammetry profile of the C(20)GCN-Scop cathode. b) Galvanostatic charge/discharge profile of prepared cell at 0.1 C, 0.2 C, 0.5 C, 1 C, and 2 C. c) Rate performance at different current densities 0.1 C, 0.2 C, 0.5 C, 1 C, 2 C, and 0.1 C. d) Galvanostatic charge/discharge voltage profile of 1<sup>st</sup>, 100<sup>th</sup>, and 1000<sup>th</sup> cycle at 1 C.

electrochemical redox reactions. A little shift in oxidation peak is observed in first few cycles due to solid electrode-electrolyte interface (SEI) formation at cathode. After few cycles, it becomes stable and the cell shows better stability in 5<sup>th</sup> and 6<sup>th</sup> cycles. In Figure 7(b), the galvanostatic charge/discharge voltage profile of prepared cell shows a pair of oxidation/reduction peaks corresponding to the lithium polysulfides which reconfirms two-step reduction and oxidation during electrochemical redox reaction as reported in CV curve. In comparison to the theoretical capacity of sulfur ( $1675 \text{ mAh g}^{-1}$ ), the cell exhibits a high reversible specific capacity of  $1387 \text{ mAh g}^{-1}$  at 0.1 C. In the charge/discharge profile, the polarization is small ( $\Delta E \sim 0.25$  V at the current rate of 0.1 C), indicating that charge transfer is quick in the prepared C(20)GCN-Scop cathode during discharge/charge. These aforementioned results of prepared cell confirm that the presence of conducting carbon-rich GCN provided the conduction path during electrochemical redox reactions, and the presence of heteroatom strengthens the interaction between host and sulfur species (sulfur and soluble intermediate polysulfides), however, optimum utilization of sulfur copolymer encapsulated in carbon-rich GCN provides high energy density.

The rate performance of the fabricated cell of synthesized C(20)GCN-Scop cathode is shown in Figure 7(c). The cell delivers initial specific capacity of  $1387$ ,  $1139$ ,  $979$ ,  $840$ , and  $614 \text{ mAh g}^{-1}$  at  $0.1$  C,  $0.2$  C,  $0.5$  C, and  $2$  C, respectively, and it again provides excellent reversible specific capacity of  $1191 \text{ mAh g}^{-1}$  at  $0.1$  C when the cell switches from  $2$  C to  $0.1$  C. The cyclic performance of the prepared cell carried out at  $1$  C shows an initial discharge capacity of  $\sim 579 \text{ mAh g}^{-1}$  in first

cycle which is increased with the increase in number of cycles and becomes  $\sim 839 \text{ mAh g}^{-1}$  after 50 cycles (Figures 7d and 8a). Since in first few cycles, due to unstable solid (electrode) electrolyte interface (SEI), the cell shows less capacity along with fluctuation in the coulombic efficiency, but once, the SEI becomes stable, the accessibility of active material becomes easier, the cell delivers high specific discharge capacity. After 1000 cycles, the prepared cell delivers reversible discharge capacity of  $\sim 700 \text{ mAh g}^{-1}$  with excellent coulombic efficiency as shown in Figure 8(a). For comparison purposes, a cell containing GCN-sulfur composite cathode and lithium metal as anode is also prepared, which initially delivers high discharge capacity ( $\sim 1107 \text{ mAh g}^{-1}$  at  $0.5$  C) than that of C(20)GCN-Scop cathode, but rapid fading in the capacity with cycle is observed due to the dissolution of sulfur and intermediate discharge product of sulfur. Since the synthesized bulk GCN has relatively low specific surface area with larger average pore diameter which means most of sulfur is deposited on the surface of GCN. As a result, in the first few cycles, it delivers high discharge capacity due to easy accessibility of surface sulfur, but, in successive cycles, the surface sulfur will easily be dissolved in electrolyte. Therefore, fast capacity fading is observed and the discharge capacity of this cell decrease to  $\sim 391 \text{ mAh g}^{-1}$  after 170 cycles. While cell prepared of C(20)GCN-Scop cathode shows much more stable cyclability as compared to GCN-sulfur cathode. The cells are decrimped in an inert environment (inside Ar-filled glovebox) after cyclability to investigate the physical state of their components. The optical image of the anode of both cells is shown in Figure S7(a and b). Large amounts of polysulfides are deposited on the anode of the cell

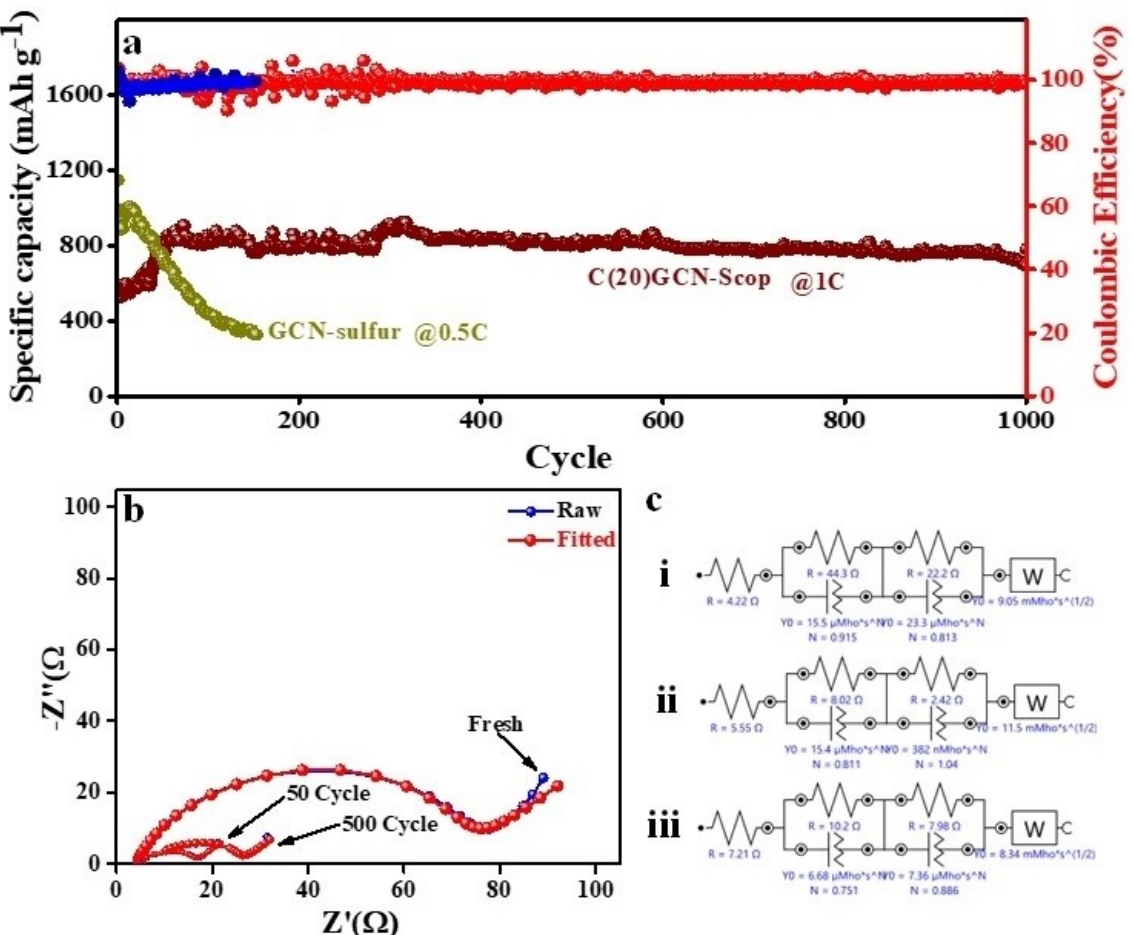


**Figure 8.** a) Cycle performance at 1 C over 1000 cycles. b) Electrochemical impedance spectra (EIS) of fresh cell, after 50 cycles & 500 cycles. c) The equivalent electrochemical circuits fitted with EIS measurement: i) fresh cell, ii) after 50 cycles, iii) after 500 cycles.

constructed with GCN-sulfur cathode (Figure S7a), but a very small amount of polysulfide deposition is detected on the lithium anode of the cell fabricated with C(20)GCN-Scop cathode (Figure S 7(b)).

To investigate the contribution of carbon-rich conducting GCN framework on the electrochemical performance of the cell, electrochemical impedance spectroscopy (EIS) is performed at open-circuit potential (OCP) of the prepared cell within the frequency range 0.1 Hz to 10<sup>4</sup> Hz at null direct current by applying a fixed direct voltage equal to OCP. The EIS of the prepared cell (Li/1.0 M LiTFSI+DME/DOL (1:1, volume ratio)+0.1 M LiNO<sub>3</sub>/C(20)GCN-Scop) is recorded before the cyclic performance, after 50 cycles, and after 500 cycles as shown in Figure 8(b). Their corresponding fitted equivalent circuit diagrams are shown in Figure 8(c). The values of resistance of electrolyte ( $R_E$ ), solid electrode-electrolyte interface resistance ( $R_{SEI}$ ), charge transfer resistance ( $R_{CT}$ ), and the Warburg impedance ( $W_0$ ) are measured from the electrochemical circuit fitting of EIS given in Table 1, 2. The value of  $R_E$  slightly increases from its initial value (4.22 Ω), after 50 cycles (5.55 Ω) and 500 cycles (7.21 Ω), which is due to dissolution of some intermediate polysulfides in the liquid electrolyte with cycle, but it is quite close to the initial  $R_E$  which indicates the low loss

**Table 1.** Elements and their weight and atomic percentage in synthesized GCN, C(20)GCN, and C(20)GCN-Scop.

Serial no.	Sample	Element	Weight [%]	Atomic [%]
1	GCN	C	37.22	41.05
		N	59.05	55.86
		O	3.73	3.09
2	C(20)GCN	C	79.75	82.42
		N	16.95	15.02
		O	3.29	2.55
3	C(20)GCN-Scop	C	14.05	29.38
		N	2.77	1.39
		O	1.19	5.00
		S	81.99	64.23

of active material with cycle. In the fresh cell, the value of  $R_{SEI}$  is high ~44.3 Ω and, after 50 cycles, it decreases to 8.2 Ω which indicates that the SEI becomes more stable with the cycle and it allows easy charge transportation between electrode and electrolyte after few cycles. This change in SEI is clearly observed in the cyclic performance of the prepared cell (Figure 8a) in which the capacity of cell increases with cycle up to 50 cycles and after that it becomes stable. For GCN-sulfur

**Table 2.** The EIS values obtained from electrochemical circuit fitting of Nyquist plots of prepared cell.

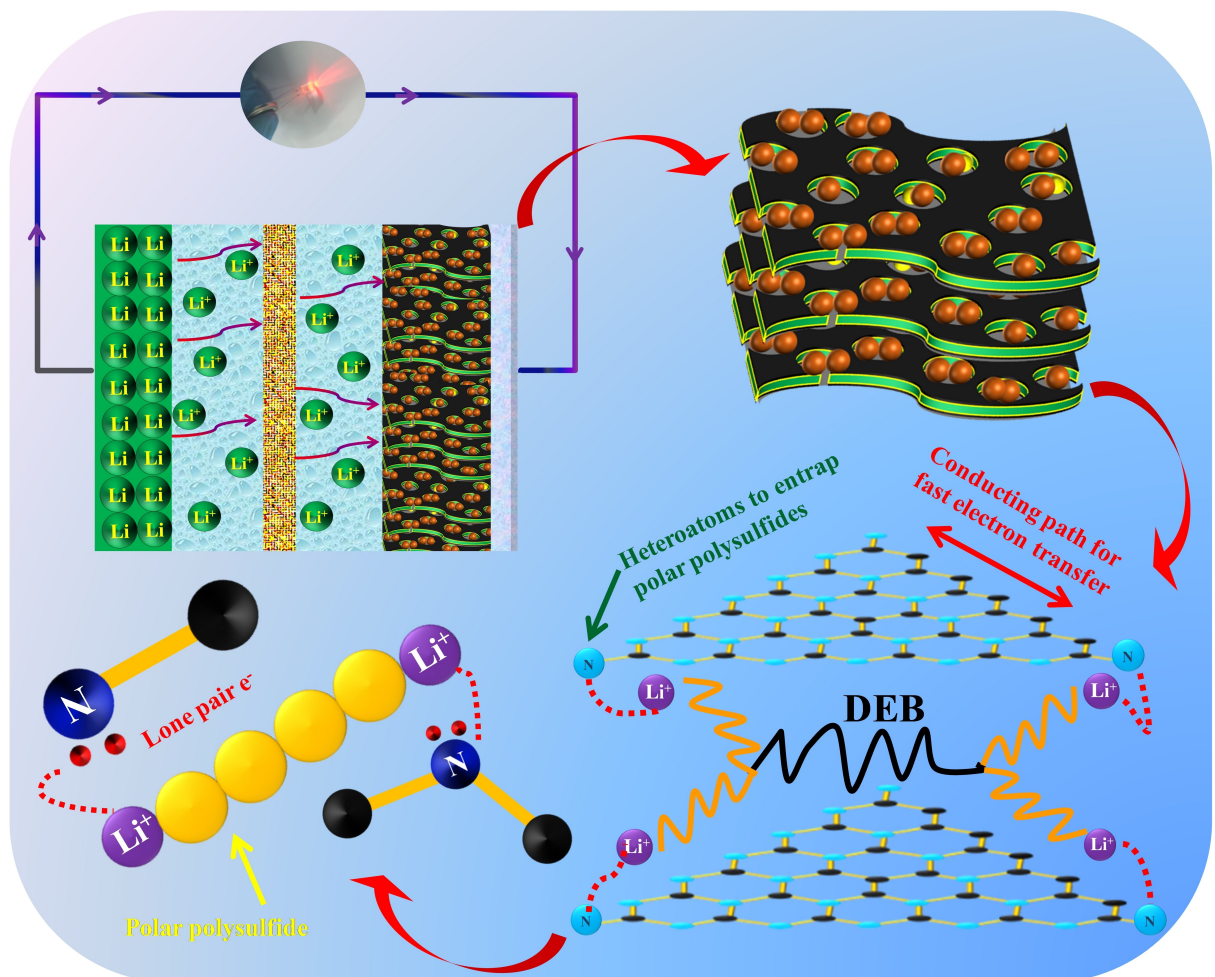
Condition	$R_e$ [ $\Omega$ ]	$R_{SEI}$ [ $\Omega$ ]	$R_{ct}$ [ $\Omega$ ]	$W_0$ [mMho $s^{1/2}$ ]
Before	4.22	44.3	22.2	9.05
After 50 cycles	5.55	8.02	2.42	11.5
After 500 cycles	7.21	10.2	7.98	8.34

cathode, the EIS spectra and corresponding fitted electrochemical circuit of the cell (Li/1.0 M LiTFSI + DME/DOL (1:1, volume ratio) + 0.1 M LiNO<sub>3</sub>/GCN-sulfur) is also shown in Figure S8 which shows higher  $R_{SEI}$  (~46.7  $\Omega$ ) and  $R_{ct}$  (~38.4  $\Omega$ ) values than the C(20)GCN-Scop. This shows electrical conductivity of synthesized C(20)GCN-Scop cathode is better than GCN-sulfur, which contributes to the maximum utilization of active material (sulfur copolymer). Role of the sulfur copolymer and carbon-rich GCN in synthesized C(20)GCN-Scop cathode through schematic representation for better LiSBs is summarized in Scheme 2. It shows that the accessibility of active material (sulfur) in porous carbon-rich conducting framework is easier for both electron and lithium-ion during electrochemical redox reactions. The nitrogen atoms present in C(20)GCN host interact with intermediate polar polysulfides and successfully suppress dissolution in electrolyte. The cell demonstrates low

EIS values and superior coulombic efficiency of ~99% throughout the cycling and rate performance. It promotes fast charge transfer (lithium-ions as well as electrons) for oxidation/reduction reactions during the process of charging/discharging which demonstrates the good rate capability of the C(20)GCN-Scop cathode. Therefore, the superior electrochemical performance of the C(20)GCN-Scop cathode material demonstrates its applicability as a promising cathode material for high-capacity rechargeable LiSBs.

## Conclusion

We have successfully developed a thermally stable, porous, and conducting carbon-rich graphitic carbon nitride host material via a facile approach of co-crystallization coupled with thermal



**Scheme 2.** Schematic working diagram of the prepared lithium-sulfur cell showing trapping of intermediate polar polysulfide by heteroatom.

pyrolysis in a controlled (inert) environment. The uniform distribution of sulfur copolymer loading throughout the carbon-rich conducting C(20)GCN host matrix is carried out for long cycle life and high-capacity cathode preparation for LiSBs. The nitrogen atoms present in carbon-rich C(20)GCN host interact with sulfur and intermediate polar polysulfides and successfully suppress dissolution in the electrolyte. The high specific surface area ( $\sim 273 \text{ m}^2 \text{ g}^{-1}$ ) of carbon-rich GCN, helps to incorporate a high amount ( $\sim 76\%$ ) of active material (sulfur copolymer) as well as lithium polysulfide, which results in a high-capacity cathode material with excellent cyclability. The cell prepared using C(20)GCN-Scop cathode demonstrates lower EIS values than the cell fabricated using GCN-sulfur composite as cathode and facilitates rapid electro-kinematics during charging and discharging of the cell. The cell prepared using C(20)GCN-Scop cathode shows a high reversible capacity  $\sim 1387 \text{ mAh g}^{-1}$  at 0.1 C ( $\sim 840 \text{ mAh g}^{-1}$  at 1 C), long cyclability up to 1000 cycles (at 1 C) along with ultra-low capacity fading ( $\sim 0.14 \text{ mAh g}^{-1}$  in each cycle, i.e., 0.016% in each cycle at 1 C).

## Experimental

### Materials

Urea (99%, 60.06 g mol $^{-1}$ ), lithium nitrate (LiNO $_3$ , 99.99%, 68.95 g mol $^{-1}$ ), citric acid (> 99.5%, 192.12 g mol $^{-1}$ ), ethylenediamine (EDA, > 99%, 60.10 g mol $^{-1}$ ), hydrochloric acid (37%, 36.46 g mol $^{-1}$ ), ethanol (absolute, 46.07 g mol $^{-1}$ ), and methanol (> 99%, 32.04 g mol $^{-1}$ ) are purchased from Merck. Dimethyl sulfoxide (DMSO, 78.13 g mol $^{-1}$ ), 1,3-diethynylbenzene (DEB, 126.15 g mol $^{-1}$ ), sulfur powder trace metal basis (99.98%, 32.07 g mol $^{-1}$ ), 1,3-dioxolane (DOL, 99%, 74.08 g mol $^{-1}$ ), dimethoxyethane (DME, 99.95%, 90.12 g mol $^{-1}$ ), lithium bis-trifluoromethanesulfonylimide (LiTFSI, 99.95%, 287.09 g mol $^{-1}$ ) and lithium metal ribbon (99.9% trace metal basis, thickness  $\sim 0.38 \text{ mm}$ , 6.94 g mol $^{-1}$ ) are purchased from Sigma Aldrich. Carbon super P (CSP), carboxyl methyl cellulose (CMC, 400,000 g mol $^{-1}$ ), aluminium foil as current collector (thickness = 15  $\mu\text{m}$ ), and celgard separator are purchased from MTI corporation. Deionized water is used during synthesis. All the above mentioned commercially purchased materials are used without any further treatment during synthesis. The materials sensitive to oxygen and moisture are stored and handled in the inert atmosphere inside the glove box (MBRAUN ABstar) filled with inert gas (Argon) under controlled value of moisture and oxygen ( $\text{H}_2\text{O} < 0.5 \text{ ppm}$ ,  $\text{O}_2 < 0.5 \text{ ppm}$ ).

### Synthesis of conducting carbon-rich GCN

The conducting carbon-rich graphitic carbon nitride (C(x)GCN, x weight (wt.)%, x=5, 10, 15 and 20) is synthesized by using urea and different amounts of citric acid, where citric acid is used as carbon source. For co-crystallization of urea and citric acid, both ingredients are dissolved in deionized water and the obtained solution is stirred for 6 h (Scheme 1a). The water is evaporated very slowly to prevent any side reaction during re-crystallization (Scheme 1b and c). Initially, in co-crystallization method, the molecules of solid molecular compounds are arranged in particular manner without any covalent interaction between molecules of citric acid and urea (Scheme 1c).<sup>[53]</sup> This co-crystallized powder is transferred to alumina crucible and heated at 550 °C for 3 h under continuous Argon (Ar) flow. Further, it is heated at 800 °C and held

for 1 h under continuous Argon (Ar) flow for the removal of side functional groups to get high conducting carbon-rich graphitic carbon nitride framework. The prepared carbon-rich graphitic carbon nitride by using 5, 10, 15, and 20 weight (wt.)% of citric acid in urea is named as C(5)GCN, C(10)GCN, C(15)GCN, and C(20)GCN, respectively. The bulk GCN is synthesized by using thermal pyrolysis method of urea precursor. Urea is placed in a semi-closed crucible and heated up to 550 °C under continuous Argon (Ar) flow at heating rate 5 °C min $^{-1}$  and it is held for 3 h at 550 °C and then cooled naturally.

### Nanosulfur loading in C(20)GCN and its copolymerization

The 100 mg of synthesized C(20)GCN is dispersed in 100 mL deionized water ( $\sim 1 \text{ mg mL}^{-1}$ ) by using ultrasonication process. Nano sulfur particles are loaded in the synthesized C(20)GCN framework by using the EDA sulfur nano-precursor technique (400 mg of sulfur in 20 mL EDA), which is based on the chemical deposition method reported in our previous work (Scheme 1d).<sup>[14]</sup> Subsequently, the loaded nano-sulfur particles are co-polymerized by adding the 1,3-Diethynylbenzene (DEB) monomer.<sup>[24]</sup> In this process, the appropriate amount of monomer DEB (15 wt.% of total sulfur amount  $\sim 60 \text{ mg}$ ) is dissolved into DMSO solvent in a semi-closed vessel. After that, nano sulfur-loaded C(20)GCN is added to the above solution and is stirred for 30 minutes. Once, a homogeneous solution is obtained, the above solution is heated up to 170 °C and this solution is kept for copolymerization of sulfur nanoparticles and DEB monomer at this temperature for 2 h. The synthesized C(20)GCN sulfur copolymer (C(20)GCN-Scop) is vacuum dried at 100 °C for 48 h to completely remove DMSO.

### Materials characterization

The crystalline and amorphous phases of synthesized materials are investigated by using X-ray diffraction (XRD) results, which is recorded by powder XRD Bruker, Model-D8 Advance (Eco) X-Ray diffraction system (Bruker Corporation) within range 10° to 80° 2Theta (degree) with 5 degree min $^{-1}$  scan rate. The thermogravimetric analysis (TGA) is investigated by METTLER TOLEDO TGA/DSC 1 to collect information about thermal decomposition of synthesized GCN, carbon-rich GCN, and actual loading of nano sulfur in composites. Fourier transform infrared (FTIR) spectrum of the prepared materials is recorded using Perkin Elmer FTIR Frontier spectrometer. The RENISHAW inVia Qontor Confocal Raman microscope is used to record Raman spectra of synthesized samples with the help of 532 nm Nd:Yag laser of  $\sim 0.3 \text{ mW}$  incident power coupled with CCD detector. The PHI 5000 VersaProbe III surface analysis scanning XPS microprobe is used to perform X-ray photo-electron spectroscopy (XPS). The structural morphologies of synthesized materials and their elemental composition are recorded by scanning electron microscopy (SEM) EVO – Scanning Electron Microscope ZEISS EVO/18 Research (CARL ZEISS MICROSCOPY LTD.) with inbuilt energy-dispersive X-ray spectroscopy (EDS) AMETEK EDAX-EDS system. The transmission electron microscopy (TEM) is performed by HR-TEM, TECNAL G2 20 TWIN (FEI USA PTE, LTD). Micromeritics Gemini VII (2390 t) is used to perform the Brunauer Emmet Teller (BET) measurement for porosity via the N $_2$  adsorption-desorption technique. All electrochemical characterizations of prepared cells (i.e., LiSB) are performed using the AUTOLAB PGSTAT 302 N (Metrohm Lab) controlled by software NOVA (2.1.3 version). The ARBIN LBT21084 battery analyser (16 channels) is used to record galvanostatic charge-discharge measurement of prepared cells.

## Lithium-sulfur cell assembly

The synthesized C(20)GCN nano-sulfur copolymer active material (80 wt.%), CMC binder (3.5 wt.%), and CSP conducting material (16.5 wt.%) are taken to prepare cathode for lithium-sulfur cell. The homogeneous aqueous slurry of above materials is prepared through vacuum mixer and is further casted on the aluminium current collector with the help of an automated thick film coater (MTI MSK-AFA-II-VC-HF). The coated cathode film is dried for 24 hours at 100 °C in a vacuum oven. The prepared cathode film is punched in discs where sulfur loading is ~2.8 mg cm<sup>-2</sup>. The lithium metal as anode and 1.0 M LiTFSI/DME + DOL (1:1 volume ratio) as electrolyte along with 0.1 M LiNO<sub>3</sub> additive have been used in cell fabrication. 0.1 M LiNO<sub>3</sub> additive helps to develop a passive layer on the anode. The CR-2032 coin cells are assembled in an argon-filled glove box. The cells are fabricated using circular discs of prepared cathode and lithium metal anode (12 mm in diameter) separated by a celgard separator, which is soaked in the prepared electrolyte solution (10 μL mg<sup>-1</sup> electrolyte sulfur ratio).

## Acknowledgements

R.K.S. thankfully acknowledges to Institute of Eminence (IoE, UGC India) for financial assistance in carrying out this research. R.K.T. is grateful to the IoE for giving him the Junior Research Fellowship.

## Conflict of Interest

The authors declare no conflict of interest.

## Data Availability Statement

The data that support the findings of this study are available from the corresponding author upon reasonable request.

**Keywords:** carbon-rich graphitic carbon nitride host · cathode · high capacity · long cycle life · nano sulfur copolymer,

- [1] X. L. Xu, S. J. Wang, H. Wang, B. Xu, C. Hu, Y. Jin, J. B. Liu, H. Yan, *J. Energy Storage* **2017**, *13*, 387.
- [2] R. Mishra, S. K. Singh, H. Gupta, N. Srivastava, D. Meghnani, R. K. Tiwari, A. Patel, A. Tiwari, V. K. Tiwari, R. K. Singh, *Appl. Surf. Sci.* **2021**, *535*, 147695.
- [3] T. Liu, H. Hu, X. Ding, H. Yuan, C. Jin, J. Nai, Y. Liu, Y. Wang, Y. Wan, X. Tao, *Energy Storage Mater.* **2020**, *30*, 346.
- [4] H. Gupta, S. K. Singh, V. K. Singh, A. K. Tripathi, N. Srivastava, R. K. Tiwari, R. Mishra, D. Meghnani, R. K. Singh, *J. Electrochem. Soc.* **2019**, *166*, A5187.
- [5] A. Eftekhari, D. W. Kim, *J. Mater. Chem. A* **2017**, *5*, 17734.
- [6] A. Rosenman, E. Markevich, G. Salitra, D. Aurbach, A. Garsuch, F. F. Chesneau, *Adv. Energy Mater.* **2015**, *5*, 1500212.
- [7] N. Srivastava, S. K. Singh, H. Gupta, D. Meghnani, R. Mishra, R. K. Tiwari, A. Patel, A. Tiwari, R. K. Singh, *J. Alloys Compd.* **2020**, *843*, 155615.
- [8] J. Zhu, P. Zhu, C. Yan, X. Dong, X. Zhang, *Prog. Polym. Sci.* **2019**, *90*, 118.
- [9] W. C. Du, Y. X. Yin, X. X. Zeng, J. L. Shi, S. F. Zhang, L. J. Wan, Y. G. Guo, *ACS Appl. Mater. Interfaces* **2016**, *8*, 3584.
- [10] X.-B. Cheng, J.-Q. Huang, Q. Zhang, *J. Electrochem. Soc.* **2017**, *165*, A6058.
- [11] J. Wang, J. Zeng, H. Li, J. Li, B. J. Hwang, Y. Zhang, J. Zhao, Y. Wang, Y. Peng, *Sci. Rep.* **2017**, *7*, 1.
- [12] A. A. Tidblad, H. Berg, K. Edström, *Swedish Hybrid Vehicle Centre* **2015**, *1*, 10-2015..
- [13] N. Angulakshmi, A. M. Stephan, *Front. Energy Res.* **2015**, *3*, 17..
- [14] R. K. Tiwari, S. K. Singh, H. Gupta, N. Srivastava, D. Meghnani, R. Mishra, A. Patel, A. Tiwari, V. K. Tiwari, R. K. Singh, *Electrochim. Sci. Adv.* **2021**, *2*, e202100025.
- [15] J. K. Kim, F. Mueller, H. Kim, S. Jeong, J. S. Park, S. Passerini, Y. Kim, *ChemSusChem* **2016**, *9*, 42.
- [16] A. A. Tidblad, H. Berg, K. Edström, *Swedish Hybrid Vehicle Centre* **2015**, *1*, 10-2015..
- [17] R. Mishra, S. K. Singh, H. Gupta, N. Srivastava, D. Meghnani, R. K. Tiwari, A. Patel, A. Tiwari, V. K. Tiwari, R. K. Singh, *Appl. Surf. Sci.* **2021**, *535*, 147695.
- [18] S. K. Singh, D. Dutta, R. K. Singh, *Electrochim. Acta* **2020**, *343*, 136122.
- [19] L. Duan, F. Zhang, L. Wang, *Alkali-ion Batteries* **2016**, *45*.
- [20] S. Xin, L. Gu, N. H. Zhao, Y. X. Yin, L. J. Zhou, Y. G. Guo, L. J. Wan, *J. Am. Chem. Soc.* **2012**, *134*, 18510.
- [21] Z. Liang, J. Shen, X. Xu, F. Li, J. Liu, B. Yuan, Y. Yu, M. Zhu, *Adv. Mater.* **2022**, *22*, 2200102.
- [22] J. Liu, S. Xiao, X. Liu, R. Wu, X. Niu, Y. Xiang, J. S. Chen, C. Yang, *Chem. Eng. J.* **2021**, *423*, 130246.
- [23] S. H. Chung, A. Manthiram, *Adv. Mater.* **2018**, *30*, 1.
- [24] A. Bhargav, J. He, A. Gupta, A. Manthiram, *Joule* **2020**, *4*, 285.
- [25] C. Li, K. Gao, Z. Zhang, *Nanotechnology* **2018**, *29*, 465401.
- [26] H. Dunya, Z. Yue, M. Ashuri, X. Mei, Y. Lin, K. Kucuk, S. Aryal, C. U. Segre, B. K. Mandal, *Mater. Chem. Phys.* **2020**, *246*, 122842.
- [27] Y. Ansari, S. Zhang, B. Wen, F. Fan, Y. M. Chiang, A. Eftekhari, D. W. Kim, *Adv. Energy Mater.* **2019**, *9*, 1.
- [28] S. Yao, S. Xue, S. Peng, M. Jing, X. Qian, X. Shen, T. Li, Y. Wang, *J. Mater. Sci. Mater. Electronics* **2018**, *29*, 17921.
- [29] Z. Chen, Z. Sun, Y. Zhang, T. Tan, Y. Tian, Z. Chen, *Nanomaterials* **2018**, *8*, 303.
- [30] L. Sun, D. Wang, Y. Luo, K. Wang, W. Kong, Y. Wu, L. Zhang, K. Jiang, Q. Li, Y. Zhang, J. Wang, S. Fan, *ACS Nano* **2016**, *10*, 1300.
- [31] M. Li, Z. Liu, Y. Zhang, X. Wang, C. Zhang, S. Zhang, *J. Solid State Electrochem.* **2021**, *25*, 1293.
- [32] C. Xiong, Y. X. Ren, H. R. Jiang, M. C. Wu, T. S. Zhao, *J. Energy Storage* **2019**, *26*, 101006.
- [33] N. Angulakshmi, R. B. Dhanalakshmi, S. Sathya, J. H. Ahn, A. M. Stephan, *Batteries & Supercaps* **2021**, *4*, 1064.
- [34] G. Zheng, Y. Yang, J. J. Cha, S. S. Hong, Y. Cui, *Nano Lett.* **2011**, *11*, 4462.
- [35] A. Ghosh, S. Shukla, G. S. Khosla, B. Lochab, S. Mitra, *Sci. Rep.* **2016**, *6*, 1.
- [36] A. Ganesan, A. Varzi, S. Passerini, M. M. Shaijumon, *Electrochim. Acta* **2016**, *214*, 129.
- [37] J. Liu, W. Li, L. Duan, X. Li, L. Ji, Z. Geng, K. Huang, L. Lu, L. Zhou, Z. Liu, W. Chen, L. Liu, S. Feng, Y. Zhang, *Nano Lett.* **2015**, *15*, 5137.
- [38] Y. Zhang, Z. Gao, N. Song, J. He, X. Li, *Mater. Today* **2018**, *9*, 319.
- [39] J. Wang, J. Yang, J. Xie, N. Xu, *Adv. Mater.* **2002**, *14*, 963.
- [40] Z. Sun, M. Xiao, S. Wang, D. Han, S. Song, G. Chen, Y. Meng, *J. Mater. Chem. A* **2014**, *2*, 9280.
- [41] V. K. Tiwari, H. Song, Y. Oh, Y. Jeong, *Energy* **2020**, *195*, 117034.
- [42] Q. Lu, Y. Zhong, W. Zhou, K. Liao, Z. Shao, *Adv. Mater. Interfaces* **2018**, *5*, 1.
- [43] L. Fan, Z. Li, W. Kang, B. Cheng, *Renewable Energy* **2020**, *155*, 309.
- [44] AR. Poorna, R. Saravanathanizhan, N. Balasubramanian, *Electrochim. Sci. Adv.* **2020**, *1*(3) e2000028..
- [45] H. M. Kim, J. Y. Hwang, A. Manthiram, Y. K. Sun, *ACS Appl. Mater. Interfaces* **2016**, *8*, 983.
- [46] A. Mentbayeva, A. Belgibayeva, N. Umirov, Y. Zhang, I. Taniguchi, I. Kurmanbayeva, Z. Bakenov, *Electrochim. Acta* **2016**, *217*, 242.
- [47] L. Ma, H. L. Zhuang, S. Wei, K. E. Hendrickson, M. S. Kim, G. Cohn, R. G. Hennig, L. A. Archer, *ACS Nano* **2016**, *10*, 1050.
- [48] M. H. Yap, K. L. Fow, G. Z. Chen, *Green Energy & Environ.* **2017**, *2*, 218.
- [49] Q. Lu, Y. Zhong, W. Zhou, K. Liao, Z. Shao, *Adv. Mater. Interfaces* **2018**, *5*, 1.
- [50] W. He, X. He, M. Du, S. Bie, J. Liu, Y. Wang, M. Liu, Z. Zou, W. Yan, H. Zhao, *J. Phys. Chem. C* **2019**, *123*, 15924.
- [51] J. F. Olorunyomi, K. Y. Chan, L. Gao, A. A. Voskanyan, C. Y. V. Li, *Microporous Mesoporous Mater.* **2018**, *259*, 255.
- [52] A. Thomas, A. Fischer, F. Goettmann, M. Antonietti, J. O. Müller, R. Schlögl, J. M. Carlsson, *J. Mater. Chem.* **2008**, *18*, 4893.
- [53] X. Fang, R. Gao, Y. Yang, D. Yan, *iScience* **2019**, *16*, 22.
- [54] P. Zhang, X. Li, C. Shao, Y. Liu, *J. Mater. Chem. A* **2015**, *3*, 3281.
- [55] J. Ma, M. Yu, H. Ye, H. Song, D. Wang, Y. Zhao, W. Gong, H. Qiu, *Mater. Chem. Front.* **2019**, *3*, 1807.

- [56] A. Patel, H. Gupta, S. K. Singh, N. Srivastava, R. Mishra, D. Meghnani, R. K. Tiwari, A. Tiwari, V. K. Tiwari, R. K. Singh, *FlatChem* **2022**, *33*, 100351.
- [57] Y. Liu, H. Guo, B. Zhang, G. Wen, R. Vajtai, L. Wu, P. M. Ajayan, L. Wang, *Batteries & Supercaps* **2020**, *3*, 1201.
- [58] Z. Meng, Y. Xie, T. Cai, Z. Sun, K. Jiang, W. Q. Han, *Electrochim. Acta* **2016**, *210*, 829.
- [59] Z. Zhang, D. G. Xiong, A. H. Shao, X. Y. Huang, Y. Huang, J. Yu, J. X. Cai, Z. Y. Yang, *Carbon* **2020**, *167*, 918.
- [60] Z. Chen, T.-T. Fan, X. Yu, Q.-L. Wu, Q.-H. Zhu, L.-Z. Zhang, J.-H. Li, W.-P. Fang, X.-D. Yi, *J. Mater. Chem. A* **2018**, *6*, 15310.
- [61] C. Wang, H. Fan, X. Ren, J. Ma, J. Fang, W. Wang, *ChemSusChem* **2018**, *11*, 700.
- [62] H. Dai, X. Gao, E. Liu, Y. Yang, W. Hou, L. Kang, *Diamond Relat. Mater.* **2013**, *38*, 109.
- [63] A. Gashi, J. Parmentier, P. Fioux, R. Marsalek, *Chem. Eur. J.* **2022**, *28*, e202103605.
- [64] Z. Yang, Y. Zhang, Z. Schnepp, *J. Mater. Chem. A* **2015**, *00*, 1.
- [65] Y. Ansari, S. Zhang, B. Wen, F. Fan, Y. M. Chiang, *Adv. Energy Mater.* **2019**, *9*, 1.
- [66] X. Fang, X. Fang, R. Gao, Y. Yang, D. Yan, *iScience* n.d., *16*, 22.
- [67] J. H. Kang, J. S. Chen, *Diamond Relat. Mater.* **2018**, *88*, 222.
- [68] B. Liu, J. Wen, H. Chen, M. Yang, Y. Liu, H. Li, *Batteries & Supercaps* **2020**, *3*, 1091.
- [69] L. Ma, H. L. Zhuang, S. Wei, K. E. Hendrickson, M. S. Kim, G. Cohn, R. G. Hennig, L. A. Archer, *ACS Nano* **2016**, *10*, 1050.
- [70] A. H. Shao, Z. Zhang, D. G. Xiong, J. Yu, J. X. Cai, Z. Y. Yang, *ACS Appl. Mater. Interfaces* **2020**, *12*, 5968.
- [71] J. Zhang, M. Huang, B. Xi, K. Mi, A. Yuan, S. Xiong, *Adv. Energy Mater.* **2018**, *8*, 1701330.
- [72] Z. Wang, Y. Dong, H. Li, Z. Zhao, H. bin Wu, C. Hao, S. Liu, J. Qiu, X. W. D. Lou, *Nat. Commun.* **2014**, *5*, 1.
- [73] L. Duan, L. Zhao, H. Cong, X. Zhang, L. Wei, C. Xue, *Small* **2019**, *15*, 1.

Manuscript received: June 23, 2022

Revised manuscript received: August 26, 2022

Accepted manuscript online: August 29, 2022

Version of record online: September 19, 2022